



Contents lists available at ScienceDirect



Catalysis Today

journal homepage: www.elsevier.com/locate/cattod

Synthesis and photocatalytic performance of yttrium-doped CeO₂ with a hollow sphere structure

Bin Xu ^{a,b,c}, Qitao Zhang ^{a,b}, Saisai Yuan ^{a,b}, Sixiao Liu ^a, Ming Zhang ^{a,c,**}, Teruhisa Ohno ^{b,d,e,f,*}

^a School of Chemistry and Chemical Engineering, Yangzhou University, Yangzhou 225002, China

^b Department of Applied Chemistry, Faculty of Engineering, Kyushu Institute of Technology, Kitakyushu 804-8550, Japan

^c Test Center, Yangzhou University, Yangzhou 225002, China

^d JST, PRESTO and ACT-C, 4-1-8 Honcho Kawaguchi, Saitama 332-0012, Japan

^e JST, ACT-C, 4-1-8 Honcho Kawaguchi, Saitama 332-0012, Japan

^f Research Center for Advanced Eco-fitting Technology, Kyushu Institute of Technology, Tobata, Kitakyushu 804-8550, Japan

ARTICLE INFO

Article history:

Received 30 March 2016

Received in revised form 25 June 2016

Accepted 25 June 2016

Available online xxx

Keywords:

CeO₂

Yttrium-doped

Hierarchical structure

Hollow sphere

Oxygen vacancy

ABSTRACT

We report a facile and novel approach to prepare yttrium-doped CeO₂ with a hollow sphere hierarchical structure by a simple hydrothermal method with cerium nitrate hexahydrate and yttrium nitrate hexahydrate as original materials and polystyrene microsphere as a soft-template. Through systematic experiments, the effects of experimental parameters such as doping and morphology on photocatalytic characteristics of the ceria were examined in detail. The morphology and element distribution of the as-prepared samples were characterized by field emission scanning electron microscopy and high-resolution transmission electron microscopy. Structure information with Rietveld refined data were obtained by using an X-ray diffractometer. Intrinsic oxygen vacancies and extrinsic oxygen vacancies caused by doping were analyzed from Raman spectra. Analyses of elements and chemical valence analysis were carried out by X-ray photoelectron spectroscopy, and changes in reactive oxygen species were determined by calculation. Based on structural information, element valence states, and the results of photocatalytic decomposition of acetaldehyde, we can draw the conclusion that Y-doped CeO₂ with a hollow sphere hierarchical structure has high photocatalytic activity, attributed to more oxygen vacancies and surface active oxygen species. Yttrium doped ceria with hollow sphere structure has a maximum rate constant of 0.0267 h⁻¹ and an oxidation quantum efficiency of 0.3610%, which are about 2 times as high as that of pure CeO₂ with octahedral structure.

© 2016 Elsevier B.V. All rights reserved.

1. Introduction

Cerium dioxide has been extensively utilized in many practical applications such as polishing materials [1–3], solar cells [4], ultra-violet light-blocking materials [5,6] and photocatalytic materials. Ceria has attracted much attention due to its well-controlled morphology, fluorite-type structure [7,8], remarkable redox properties

and prominent oxygen storage [9,10] and release capacity (OSC) via facile conversion between Ce⁴⁺ and Ce³⁺ oxidation states [11,12].

Recently, CeO₂-based materials with different morphologies have been synthesized by various methods including thermal evaporation [13], coprecipitation [14], and the sol-gel technique [15–17]. Previous studies have shown that excellent catalytic performance and easy functionalization of CeO₂ materials can be achieved by controlling their structural properties [18–22]. The use for morphology-controlled and size-controlled [23–25] metal and metal oxide composites [26,27] and ionic doping [28–30] are the most commonly utilized methods for enhancing the photocatalytic properties of CeO₂-based materials. The keypoint in these approaches is changing the oxygen vacancy concentrations of products, because oxygen vacancies can act as electron and hole capture centers and can trap the photogenerated electrons or

* Corresponding author at: Department of Applied Chemistry, Faculty of Engineering, Kyushu Institute of Technology, 804-8550 Kitakyushu, Japan.

** Corresponding author at: School of Chemistry and Chemical Engineering, Yangzhou University, Yangzhou 225002, China.

E-mail addresses: lxzhangm@yzu.edu.cn (M. Zhang), tohno@che.kyutech.ac.jp (T. Ohno).

holes excited by ultraviolet or visible light [33–36]. Further oxygen vacancies can effectively restrain the recombination of electron-hole pairs [37–39], resulting in improvement of photocatalytic activities [31,32].

Ceria with a sphere structure possess high oxygen storage ability, high thermal stability [41,42], good conductivity [38] and other good electrochemical performances [39,40]. In the past few decades, various morphologies of ceria including octahedral, cubes, wires and rods as well as other special one-dimensional (1D) or two-dimensional (2D) morphologies have been investigated. The main fabrication methods are hydrothermal methods with surfactants and modifying agents. Our group has fabricated yttrium-doped ceria with hedgehog-like [43] and porous broom-like [44,45] hierarchical structures by using a template-free hydrothermal process.

Hollow spheres have attracted tremendous of potential applications [46], and various strategies have been used for the fabrication of hollow spheres, including template-assisted and template-free strategies. To the best of our knowledge, however, there has been no report on the use of pure polystyrene (PS) to prepare yttrium-doped ceria hollow spheres. Herein, we report a facile and feasible approach to prepare yttrium-doped CeO₂ with a hollow sphere structure by hydrothermal technique using the simple inorganic salts Ce(NO₃)₃ and Y(NO₃)₃ as original materials and polystyrene as a soft template. The photocatalytic performance of the products was compared through systematic experiments on acetaldehyde photocatalytic oxidation.

2. Experimental section

2.1. Materials

Yttrium nitrate hexahydrate (Y(NO₃)₃·6H₂O), cerium nitrate hexahydrate (Ce(NO₃)₃·6H₂O) polyvinyl pyrrolidone (PVP) and azodiisobutyronitrile (AIBN) were of analytical grade and were used without any further purification. The original materials were purchased from Wako Co., Ltd. The size and surface electrical properties of the microsphere were analysis by the zeta potential.

2.2. Preparation

2.2.1. Preparation of polystyrene (PS) microsphere aqueous solutions

PVP were dissolved in a solution of alcohol and water, and the mixture was poured into a 250 ml four-neck flask with thermometer, mixer and condenser tube. Styrene monomer and AIBN as an initiator were added into the above mixture during the steering process. After being swept with nitrogen 30 min with, the four-neck flask was placed in an oil bath at 70 ° centigrade and the mixture was allowed to react for six hours. A polystyrene emulsion was prepared by centrifugation. After washing with an ethanol/water mixed solvent three times, the polystyrene emulsion was dispersed with water. Finally, a PSt suspension was obtained. PSt microspheres with different diameter could be obtained by controlling the concentrations of styrene monomer and AIBN initiator.

2.2.2. Yttrium-doped CeO₂ preparation

Yttrium-doped CeO₂ with a hollow sphere structure was fabricated by the traditional hydrothermal process. First, 0.87 g cerium nitrate (Ce(NO₃)₃·6H₂O) and 0.07 g yttrium nitrate (Y(NO₃)₃·6H₂O) were dissolved in 100 ml of deionized water with vigorous magnetic stirring for 30 min at room temperature. Based on the optimum dopant concentration determined in previous studies [45], we used the optimal mole ratio of 1:0.1 for cerium nitrate and yttrium nitrate. Then 0.5 ml–2 ml of polystyrene (PS) microsphere

with different diameters solutions were added to the aqueous solution. The mixture was stirred continuously for one hour. The mixed solution was then sealed in a Teflon-lined autoclave and heated at 150 °C for 24 h. After cooling to room temperature, a light yellow precipitate was collected by centrifugation and washed several times with deionized water and ethanol. Target products were obtained after drying in the air at 60 °C for one day. Yttrium-doped ceria with hollow structure was obtained by calcination of the as-prepared precursor in air at 400 °C for 4 h.

2.3. Characterization

An X-ray diffractometer (XRD) (Bruker-AXS, D8 ss) with Cu Kα radiation ($\lambda = 1.5406 \text{ \AA}$) and a monochromator was used to identify the crystalline phase. Crystallite parameters and size were calculated by the Rietveld method (TOPAS 4.0). N₂ adsorption and desorption isotherms were recorded at 77 K using a Nova 4200e instrument. The samples were precisely weighted and degased at 373 K for 3 h. The specific surface area was calculated by the 5 points Brunauer-Emmett-Teller theory. Raman analysis (Renishaw, In via) was performed using a 532 nm excitation laser with 5 mW and an air-cooled CCD detector. Raman peak shifts were determined by fitting with the Lorentzian and Gaussian composite function. Morphology and size of as-fabricated products were examined by using a field emission scanning electron microscope (FESEM) (Hitachi, S-4800, 15KV), high-resolution transmission electron microscope (HRTEM) and HADDF-STEM (FEI, Tecnai G2 F30 S-TWIN, 300KV). An inductively coupled plasma atomic emission spectrum (ICP-AES) (Shimadzu, ICPS-8000) was used to determine stability of the yttrium in the solution. An x-ray photoelectron spectroscopy (XPS) experiment was carried using a Shimadzu KRATOS AXIS-NOVA system at room temperature under 10⁻⁹ pa with Al K α radiation and C 1 s peak (83.8 eV) reference.

2.4. Photocatalytic evaluations

A UV lighter using black light (UVP, XX-15BLB) can be used to remove possible organic materials adsorbed on the surfaces of samples more than one week before evaluation of photocatalytic activity. The photocatalytic activity of as-fabricated samples was assessed by their ability for decomposition of acetaldehyde. The instruments used for catalytic activity analysis are shown in Fig. S1. Twenty milligrams of powder was spread on the bottom of a glass dish, and the glass dish was placed in a Tedlar bag (AS ONE Co. Ltd.). Five hundred ppm of acetaldehyde was injected into the bag together with 125 cm³ of artificial air. Then the bag was put in a dark place at room temperature for 2 h for reaching adsorption equilibrium. A light-emitting diode (LED; Epitex, L365), which emitted light at wavelengths of ca. 365 nm, was used as a light source, and its intensity was controlled at 0.9 mW cm⁻². The concentration of generated CO₂ as a function of irradiation time was monitored by a gas chromatograph (Shimadzu GC-8A, FID detector) equipped with a Porapak N-packed column and a methanizer (GL Science, MT-221).

3. Results and discussion

3.1. Morphology characterization

The morphology of the products was investigated by using an FE-SEM (Fig. 1) and HR-TEM (Fig. 2). Fig. 2(a) shows a panoramic view of fabricated particles. It can be seen that the particles are uniform octahedral particles with diameters of approximately 200 nm. The lattice spacing of the parallel fringes is 0.313 nm, corresponding to the (111) plane of FCC CeO₂ (inset image of Fig. 2(a)). After doping, there was no obvious change in the morphology of products,

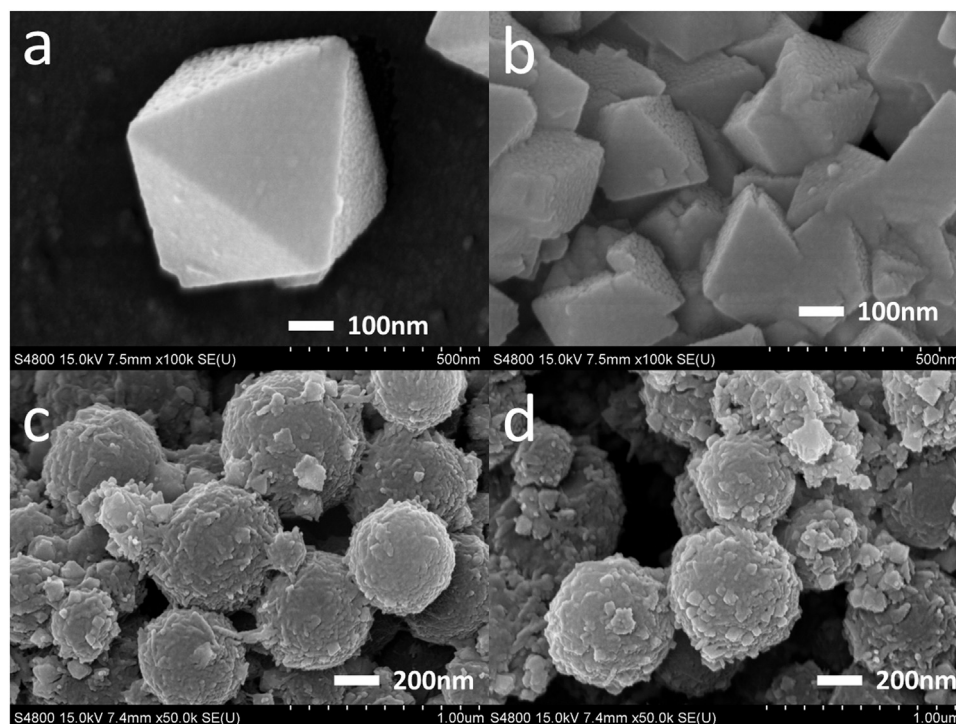


Fig. 1. FE-SEM images of the products: (a) pure CeO_2 with an octahedral structure, (b) yttrium-doped CeO_2 with an octahedral structure, (c) yttrium-doped CeO_2 with a sphere structure and (d) yttrium-doped CeO_2 with a hollow sphere structure.

and an octahedral structure and monodispersity are well maintained (Fig. 1(b)). The particle size was also about 100 nm and the exposed crystal plane was still (111). However, the inset image of Fig. 2(b) indicated that the lattice spacing of the parallel fringes is 0.314 nm, which is larger than that before doping. The composition of elements and distribution of the as-fabricated products obtained under different experimental conditions were analyzed by STEM-HAADF images and EDS mapping images. The image in Fig. 3 shows the existence of not only cerium but also yttrium, with yttrium ions being dispersed evenly on the CeO_2 octahedral structure surface and in the bulk. Herein we can draw a conclusion that yttrium enters the lattice and successfully dopes the parts of cerium. The results for composition of elements and distribution are consistent with the results of XRD and Raman analysis.

Fig. 1(c) shows that, by adding PS spheres, the morphology of the product changed to a sphere structure with diameters of approximately 300 nm. Fig. 2(c) shows that octahedral CeO_2 particles with an average diameter of 30 nm covered the PS sphere surface through electrostatic adsorption. The negative charge on the PS surface can easily capture Ce^{3+} and Y^{3+} via electrostatic interaction. Cerium and yttrium ions adsorbed on the PS surface could not generate a large crystal core due to the existence of a space steric effect. Therefore, the sizes of particles were smaller than those without PS assistance.

Figs. 1 (d) and 2 (d) show that the morphology of products is maintained as a sphere structure after calcination at 500 °C for 4 h. At same time, the diameters of spheres are about 300 nm, similar to the diameters before calcination. Thus, removal of the template does not have an influence on the morphology and size of final products. A hollow structure can be clearly observed from contact between the dark margins and the pale center in Fig. 2(d). Moreover, it reveals that the size of hollow is about 250 nm, being consistent with the PS microsphere diameter. An EDS mapping image (see Fig. 3) shows that the difference before and after calcination is elemental carbon.

3.2. Structure characterization

Typical X-ray diffractometer (XRD) patterns of samples obtained under different conditions are shown in Fig. 4. Characteristic peaks at about 28.5, 33.0, 47.4 and 56.3 2θ are attributed to pure cerium oxide with a cubic fluorite structure (JCPDS No. 34-0394) and are assigned to the crystal planes (111), (200), (220) and (311), respectively (Fig. 4(a)). The sharp diffraction peaks from all samples suggest a high degree of crystallinity of fabricated samples, and no impurity peaks appeared. The relative intensity of each peak did not change, suggesting that there is no preferred orientation. The elaborated XRD pattern of the highest peak (Fig. 4(b)) reveals that, compared with pure ceria, the highest peak position (111) of the products exhibited an obvious shift to a lower angle after yttrium doping and reached about 28.43° (2θ), indicating that the crystal lattice has expanded conspicuously due to the entry of yttrium into the crystal structure. At the same time, a PS amorphous peak around 20° (2θ) can be detected from the diffraction pattern of yttrium-doped ceria/ps. Rietveld refinements were also carried out according to the diffraction lines by varying parameters in order to investigate the actual doping quantity and location (Fig. S2). It is known that each cerium particle is arranged in a face-centered cubic surrounded by eight oxygen elements in the cubic fluorite structure of cerium dioxide. Meanwhile, oxygen elements occupy all of the tetrahedral positions and each oxygen element has four ligancy of cerium cations. When the amount of the dopant was changed without changing the other experimental conditions, there were significant changes in the lattice parameters. The lattice parameter value (a) changed to 5.4217 Å. It can be clearly seen that the lattice parameter value (a) after doping is larger than the bulk CeO_2 lattice parameter value $a = 5.4178 \text{ \AA}$ even though the space group is still Fm-3 m before and after doping. This indicates that yttrium has partially substituted cerium ions and has been introduced into the interior lattice, maintaining the ceria cubic fluorite structure instead of forming a Y_2O_3 - CeO_2 composite. Consequently, the crystal lattice would expand due to an increase in

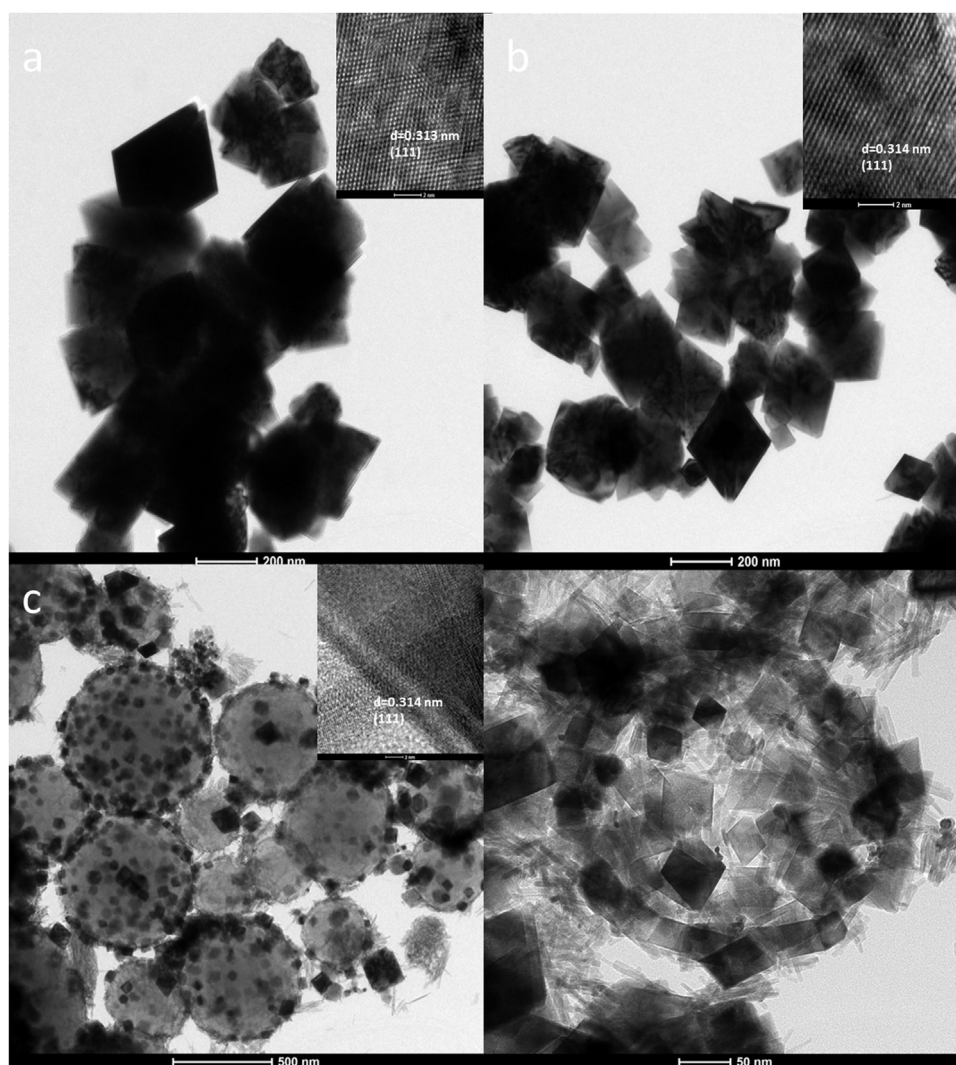


Fig. 2. HR-SEM images of the products: (a) pure CeO_2 with an octahedral structure, (b) yttrium- doped CeO_2 with an octahedral structure, (c) yttrium-doped CeO_2 with a sphere structure and (d) yttrium-doped CeO_2 with a hollow sphere structure.

oxygen vacancy concentration with an increase in yttrium content, due to the fact that the ionic radius of yttrium is larger than that of cerium (1.019 and 0.97 Å, respectively).

Raman spectra of as-fabricated samples under various experimental conditions are shown in Fig. 5. A strong Raman shift at $\sim 460 \text{ cm}^{-1}$ and a relatively weak shift at $\sim 600 \text{ cm}^{-1}$ can be detected. The shift at $\sim 460 \text{ cm}^{-1}$ can be assigned to F2g vibration of the fluorite-type structure and it can be considered as the symmetric stretching mode of oxygen atoms around cerium ions, and the molecule retains its tetrahedral symmetry throughout. Based on the results of previous studies and our own studies [43–45], a weak and less prominent band near $\sim 600 \text{ cm}^{-1}$ can be attributed to a nondegenerate longitudinal optical mode caused by a local Ce-O ($\text{R}_{\text{Ce}-\text{O}}$) bond symmetry stretch. According to previous reports, not all cerium ions show Ce^{4+} chemical valence in the lattice; small cerium ions show Ce^{3+} tervalence [44,45]. In order to maintain the particles in an electrically neutral state, the lattice oxygen would escape from the structure and finally result in the formation of intrinsic oxygen vacancies. Oxygen vacancies perturb the local Ce-O bond symmetry. A new and weak Raman shift at $\sim 530 \text{ cm}^{-1}$, which cannot be detected in Raman spectra of pure CeO_2 , can be detected. It is attributed to extrinsic oxygen vacancies caused by doping. As a dopant, yttrium enters the cubic fluorite lattice of CeO_2 and substitutes cerium. In order to maintain electronic neutrality, doping

cations showing different valence states with Ce^{4+} and part of the oxygen would also escape from the lattice to form extrinsic oxygen vacancies. The relativity intensities of Raman shifts of F2g, R_{dopant} and $\text{R}_{\text{Ce}-\text{O}}$ can be calculated from Eq. (1) [29]:

$$\frac{\text{Oxygen vacancies}}{\text{F2g}} = \frac{(\text{Aera}_{\text{R}_{\text{Ce}-\text{O}}} + \text{Aera}_{\text{R}_{\text{dopant}}})}{\text{Aera F2g}}. \quad (1)$$

The values are summarized in Table 1. It can be seen that the value of oxygen vacancies rapidly increased compared with that of pure CeO_2 after yttrium doping. This change in the value can be attributed to the amount of the dopant. When yttrium was introduced into bulk CeO_2 , more extrinsic oxygen vacancies were obtained except intrinsic oxygen vacancies. Therefore, the value of oxygen vacancies rapidly increased. Meanwhile, the value of oxygen vacancies did not show an obviously change after introduction of PS microsphere and removal of a soft template. Hence, oxygen vacancy is mainly influenced by dopant type and concentration. These results of Raman analysis are consistent with the results of XPS O_{1s} analysis and activity evaluation.

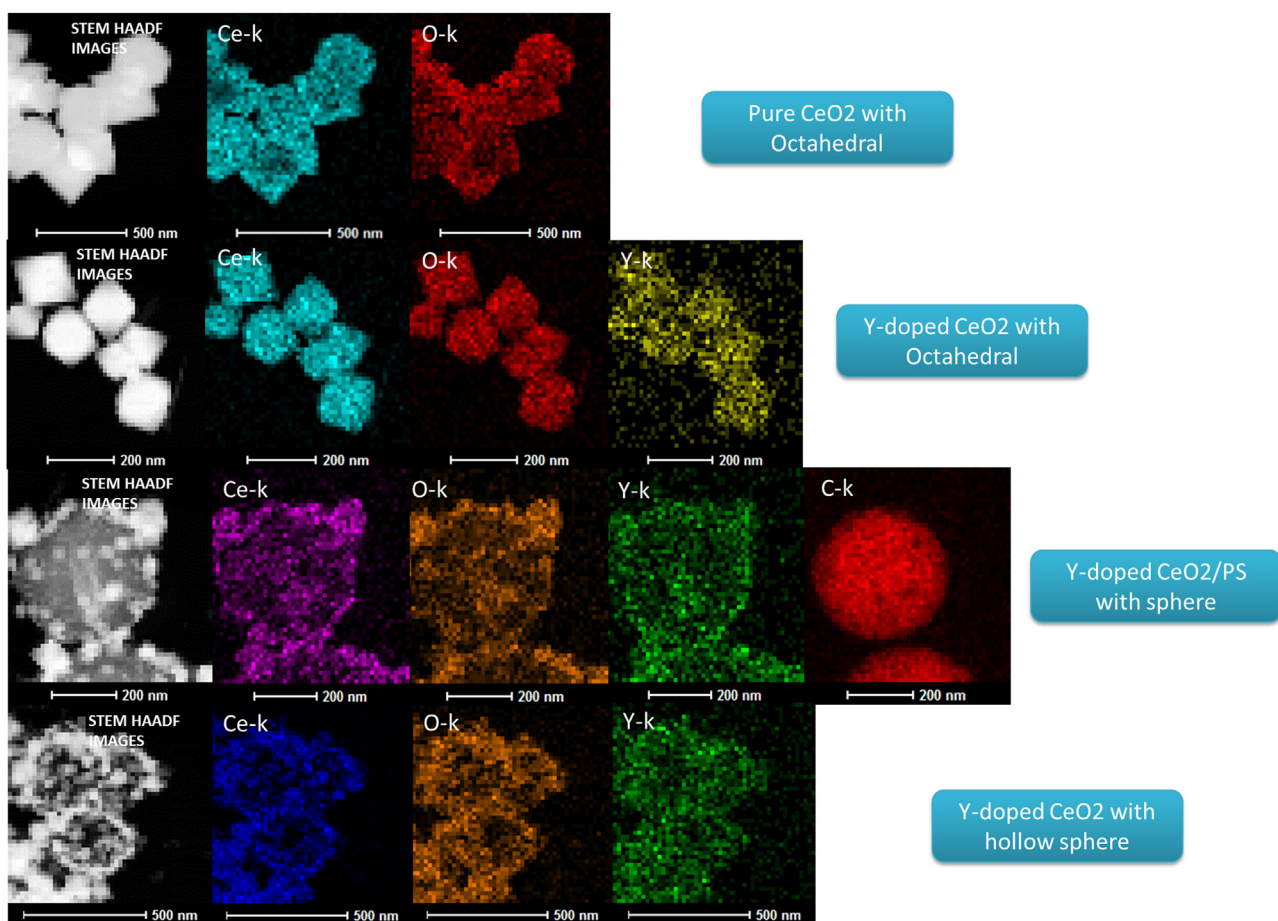


Fig. 3. HAADF images and element distribution maps of the products with different morphologies before and after doping.

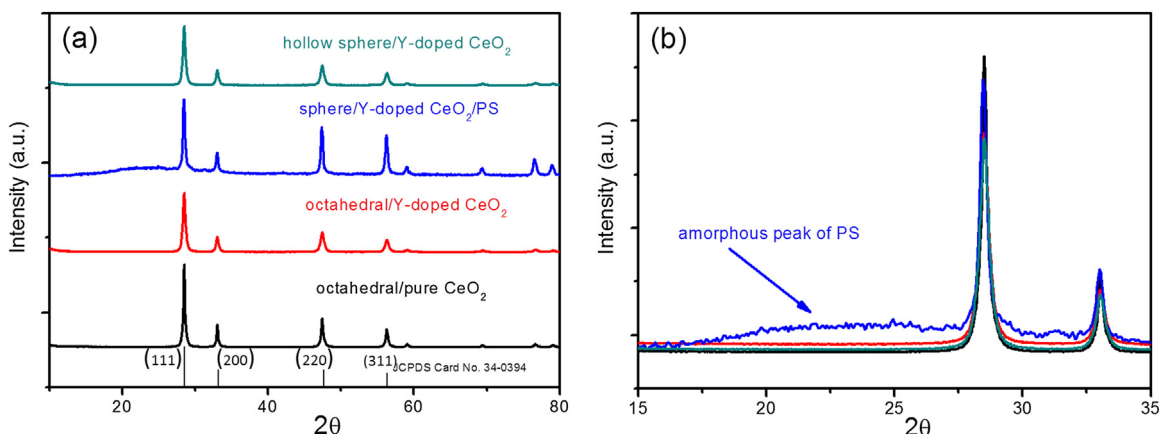


Fig. 4. XRD patterns of as-fabricated samples: (a) whole range and (b) elaborated XRD pattern of the highest peak (111).

Table 1
Rietveld refined data from XRD patterns and oxygen vacancy values calculated by Raman spectra.

sample	Lattice value a (Å)	Calculated grain size (nm)	R _{wp}	S _{BET} (m ² /g)	Area _{Oxygen vacancies} /Area _{F2g} (%)
CeO ₂ /octahedral	5.4178	4.50	5.42	35.35	1.1
Y-doped CeO ₂ /octahedral	5.4217	4.6	5.63	40.94	4.9
Y-doped CeO ₂ /PS/sphere	5.4211	4.52	5.76	78.99	5.3
Y-doped CeO ₂ /Hollow sphere	5.4215	4.54	5.97	115.34	5.8

PS: Area_{Oxygen vacancies}/Area_{F2g} (%) = (Area_{Rdoped} + Area_{Rce-o})/Area_{Fag}(%).

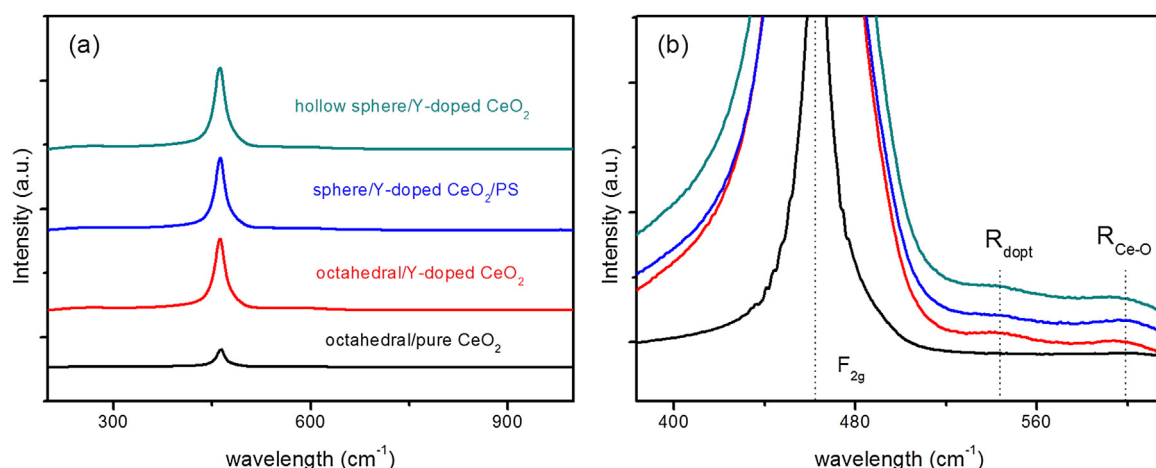


Fig. 5. Raman spectra of as-fabricated samples: (a) whole range and (b) elaborated Raman shift.

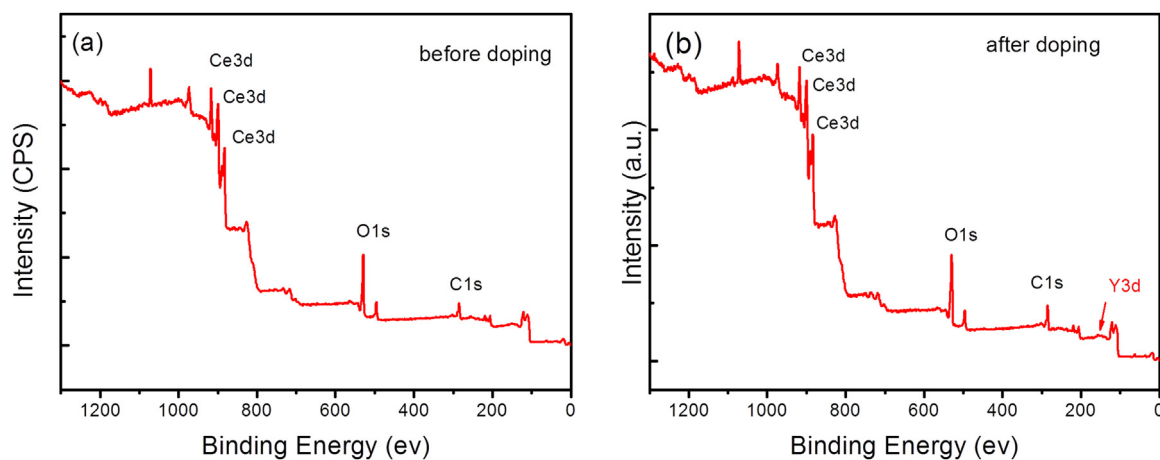


Fig. 6. Wide scanning XPS spectra of products: (a) before doping and (b) after doping.

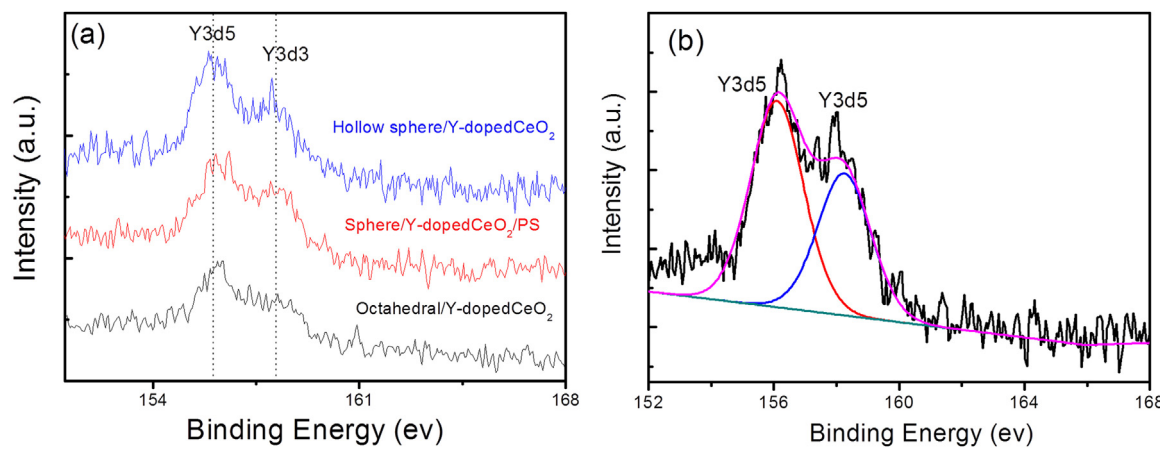


Fig. 7. High-resolution XPS spectra of Y3d (a) different morphology and (b) separated peak curve.

3.3. X-ray photoelectron spectroscopy characterization

XPS characterization was applied to determine the CeO₂ nanoparticles before and after yttrium doping. Wide scanning XPS spectra of the product is shown in Fig. 6. The elements Ce, O, and C can be detected in Fig. 6(a), and they are assigned to Ce3d, O1s and C1s binding energies, respectively. Not only the above elements but also yttrium element can be detected from the spectra, and it

is assigned to Y3d binding energy, indicating that doping was successful (Fig. 6(b)). Elaborated Y3d XPS spectra of the products after doping are shown in Fig. 7. After deconvolution and separation, two peaks located at 156.1 eV and 158.2 eV, assigned to Y3d_{5/2} binding energy, can be found from XPS profiles (Fig. 7(b)). After calculating the two peaks of Y3d, yttrium concentration in the crystal structure can be detected (Fig. 7(a)). A similar peak area indicates the approximate concentration of doping.

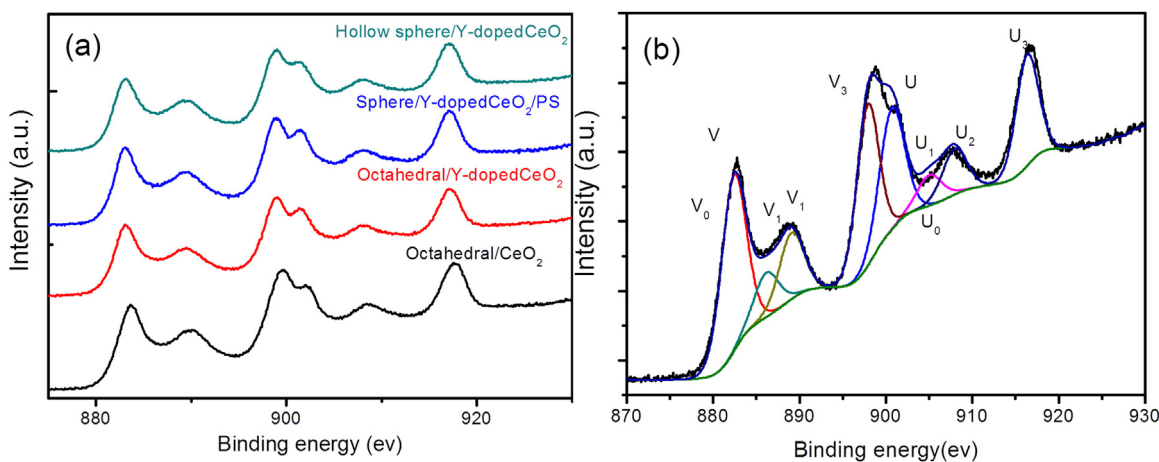


Fig. 8. High-resolution XPS spectra of Ce3d (a) different morphology and (b) separated peak curve.

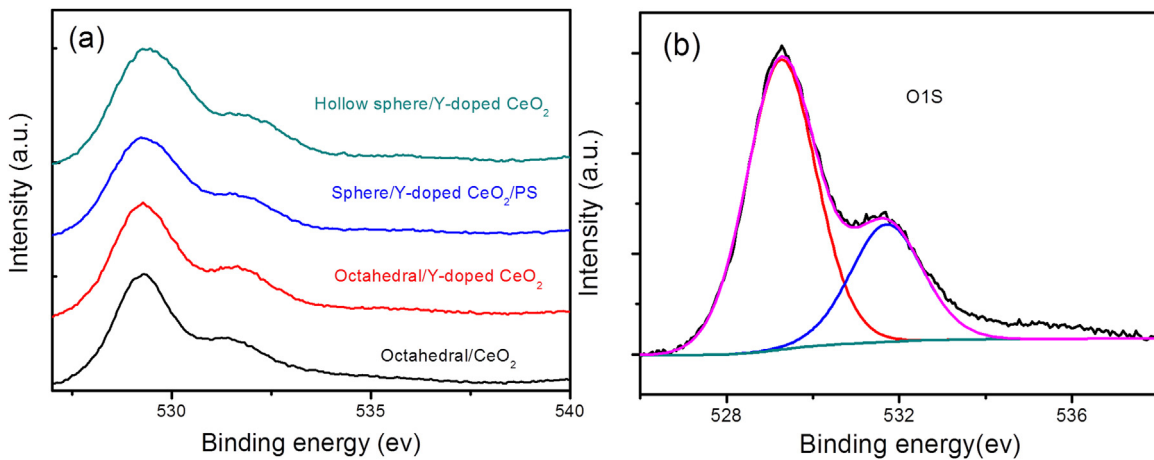


Fig. 9. High-resolution XPS spectra of O1s (a) different morphology and (b) separated peak curve.

Fig. 8 shows Ce 3d electron core level XPS spectra for as-fabricated samples and changes in Ce 3d_{3/2} and Ce 3d_{5/2} components depending on the Ce³⁺ and Ce⁴⁺ oxidation states. Five pairs of doublets, (u, v), (u₁, v₁), (u₂, v₂), (u₃, v₃) and (u₀, v₀), can be decomposed from the origin region, where u and v come from Ce 3d_{3/2} and Ce 3d_{5/2} states, respectively. We observed that (u, v), (u₂, v₂) and (u₃, v₃), which were attributed to Ce 3d⁹ 4f² O 2p⁴, Ce 3d⁹ 4f¹ O 2p⁵ and Ce 3d⁹ 4f⁰ O 2p⁶ final states, respectively, all belonged to the Ce⁴⁺ oxidation state. The two pairs of doublets (u₁, v₁) and (u₀, v₀) originated from the Ce 3d⁹ 4f¹ O 2p⁴ and Ce 3d⁹ 4f¹ O 2p⁵ final states, respectively, which correspond to the Ce³⁺ oxidation state. The relative amount of cerium in the tervalent oxidation state can be calculated from Eq. (2):

$$\frac{[\text{Ce}^{3+}]}{[\text{Ce}^{3+} + \text{Ce}^{4+}]} = \frac{\text{area}(\text{V}_0, \text{V}_1, \text{U}_0, \text{U}_1)}{\text{total area}}. \quad (2)$$

The fitted data demonstrated that the as-fabricated samples exhibit variation of [Ce³⁺] concentration. The [Ce³⁺] concentration after doping was larger than that without doping. However, although the morphology changed from an octahedral structure to a hollow sphere, [Ce³⁺] concentrations were similar after doping. Results for cerium trivalence ions and surface active oxygen are summarized in Table 2.

Fig. 9 shows O1s electron core level XPS spectra. One peak around 529.0 eV with a shoulder around 531.5 eV can be clearly seen, and they can be attributed to lattice oxygen (O_{lat}) and sur-

face active oxygen (O_{sur}), respectively. After doping, the O_{lat} and O_{sur} binding energy obviously shifted to a high energy, while the effects on O_{lat} and O_{sur} were different. The O_{sur}'s binding energy value shows a change of 0.8 eV. However, the O_{lat}'s binding energy value shows a change of only 0.2 eV. Therefore, doping of yttrium mainly affects the ceria's surface oxygen binding energy, improving the surface oxygen binding energy and enhancing the activity of surface oxygen. After deconvolution and multiple-peak separation, we could obtain the surface oxygen ratio from the Eq. (3):

$$\frac{[\text{O}_{\text{sur}}]}{[\text{O}_{\text{sur}} + \text{O}_{\text{lat}}]} = \frac{\text{area}(\text{O}_{\text{sur}})}{\text{total area}}. \quad (3)$$

The [O_{sur}] concentration after doping is larger than that without doping. There was a similar phenomenon with [Ce³⁺], although the morphology had changed from an octahedral structure to a hollow sphere, [O_{sur}] and [O_{lat}] concentrations were closed to each other after doping. The cerium trivalence and activity oxygen concentrations of the products can directly reflect the amount and activity of oxygen vacancies and suggest that yttrium-doped CeO₂ with a hollow structure should have higher catalytic activity.

3.4. Photocatalytic activity for acetaldehyde decomposition

The photocatalytic activities of the prepared samples were evaluated by CO₂ liberation from photocatalytic degradation of acetaldehyde. **Fig. 10(a)** shows liberation from acetaldehyde decomposition of as-fabricated samples. Compared with pure

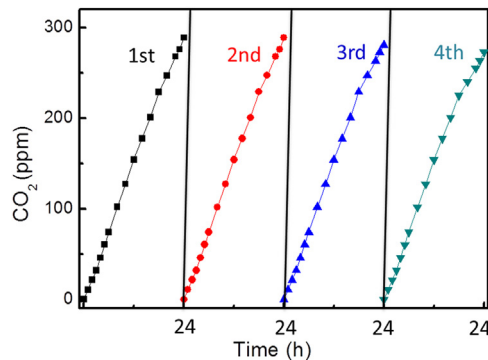
Table 2Calculated $[Ce^{3+}]$ and $[O_{sur}]$ concentrations of as-fabricated samples from the XPS spectrum.

sample	$[Ce^{3+}]/[Ce^{3+} + Ce^{4+}] \%$	$[O_{sur}]/[O_{sur} + O_{lat}] \%$
CeO ₂ /octahedral	12.60	28.53
Y-doped CeO ₂ / octahedral	21.38	33.81
Y-doped CeO ₂ / PS/sphere	23.06	39.18
Y-doped CeO ₂ / Hollow sphere	23.43	39.48
	$\frac{[Ce^{3+}]}{[Ce^{3+} + Ce^{4+}]} = \frac{\text{area}(V_0, V_1, U_0, U_1)}{\text{total area}}$	$\frac{[O_{sur}]}{[O_{sur} + O_{lat}]} = \frac{\text{area}(O_{sur})}{\text{total area}}$

Table 3

Pseudo-first-order rate constant for acetaldehyde photocatalytic oxidation under different photocatalysts and oxidation quantum efficiency of as-fabricated samples.

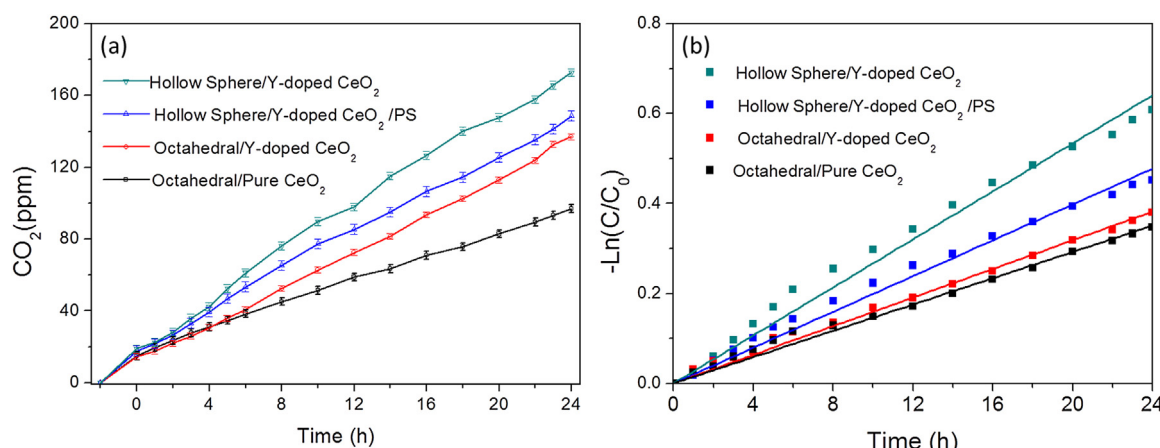
sample	The first order kinetic equation	$K(h^{-1})$	R ²	oxidation quantum efficiency
CeO ₂ /octahedral	$-\ln(C/C_0) = 0.0145t$	0.0145	0.9963	0.2043%
Y-doped CeO ₂ /octahedral	$-\ln(C/C_0) = 0.0145t$	0.0145	0.9976	0.2842%
Y-doped CeO ₂ /PS/sphere	$-\ln(C/C_0) = 0.0199t$	0.0199	0.9956	0.3115%
Y-doped CeO ₂ /Hollow sphere	$-\ln(C/C_0) = 0.0267t$	0.0267	0.9945	0.3610%

**Fig. 10.** (a) Time course of CO₂ liberation from acetaldehyde decomposition of as-fabricated samples and (b) kinetic fit for the degradation of acetaldehyde with as-fabricated samples.

CeO₂, the amount and liberation rate were significantly improved after yttrium doping, indicating that photocatalytic activities were enhanced. These results are attributed to that more oxygen vacancies and trivalent cerium produced in the ceria crystal structure. The higher the concentrations of oxygen vacancies and trivalent cerium are, the higher are the photocatalytic activities of products. From Fig. 10(a), we also can see that this kind of increase in activity was caused by yttrium doped and porous structure rather than the error of measurement. After measured CO₂ liberation amount, we calculated the oxidation quantum efficiency for synthesis products.

Yttrium doped ceria with hollow sphere structure has a maximum oxidation quantum efficiency of 0.3610%, which are about 2 times as high as that of pure CeO₂ with octahedral structure (0.2042%). The oxidation quantum efficiency values are summarized in Table 3.

Fig. 10(a) also shows that yttrium doped-CeO₂ with different morphologies exhibited different photocatalytic activities. Yttrium-doped CeO₂ with a hollow sphere structure possess higher photocatalytic activities than CeO₂ with an octahedral structure, due to the fact that small particles were fabricated in the spherical structure and a higher specific surface area was obtained. A higher specific surface area and small nanoparticles can provide more activity spots where redox reaction takes place. At the same time, yttrium dopant can provide more oxygen vacancies than without doping. When fabricated samples are irradiated by UV light, electrons are excited from the O_{2p} valence band to the conduction band (Ce_{4f}), resulting in the formation of hole and electron pairs. More surface oxygen vacancies exist on the surface of the products, and the surface oxygen-deficient site can interact strongly with exoteric oxygen molecules to form O₂⁻, O₂⁻ is an efficient electron scavenger which can trap the photogenerated electrons and then form two O⁻. The formation of O⁻ is considered to be very important for photocatalytic oxidation process. Meanwhile, the holes easily get trapped on the oxygen ions. When the number of oxygen vacancies is larger, the oxygen ion mobility becomes higher. Transportation mobility of lattice oxygen ions is beneficial for the separation of photogenerated electrons and holes [43–45]. In another word, the recombination of photogenerated electrons and holes is restricted at a higher oxygen vacancy. Therefore, yttrium-doped CeO₂ with

**Fig. 11.** Cycling runs of photocatalytic activity evaluation of yttrium-doped CeO₂ with a hollow sphere hierarchical structure.

a hollow sphere structure exhibit higher photocatalytic activities than ceria with other traditional structures.

The photocatalytic degradation kinetics of acetaldehyde was investigated, and the results were shown in Fig. 10(b). From Fig. 10(b), we can see that the changes of acetaldehyde concentration vs reaction time over the products followed pseudo-first-order kinetics plot by the equation of $-\ln(C/C_0)=kt$, where k is the pseudo-first-order rate constant, C_0 and C are the acetaldehyde concentrations at time 0 and t , respectively. After data fitting we found that reaction constant were consistent with acetaldehyde concentration changes, indicating acetaldehyde oxidation process complied with the Langmuir-Hinshelwood rate law [47,48]. Fig. 10(b) shows that yttrium-doped products reveal higher rate constants than those without doping. At same time, in those yttrium-doped products, with hollow sphere structure show higher rate constants than with octahedral structure. Yttrium doped ceria with hollow sphere structure has maximum rate constant of 0.0267 h^{-1} which is almost 2 times as high as that of pure CeO_2 with octahedral structure. The pseudo-first-order constant and relative coefficients are summarized in Table 3.

In order to investigate the photocatalytic reusability and stability of as-fabricated yttrium-doped CeO_2 with a hollow sphere structure, periodic photocatalytic decomposition experiments were performed. Fig. 11 shows cycling runs of photocatalytic activity evaluation. The photocatalytic performance of the sample had no detectable loss after four recycles and the CO_2 generation rate did not obviously change. Therefore, we can draw a conclusion that yttrium-doped CeO_2 with a hollow sphere structure possess good photocatalytic reusability as well as excellent stability.

4. Conclusion

Yttrium-doped CeO_2 with a hollow sphere hierarchical structure was successfully prepared by a simple hydrothermal method with PS as a soft template. The method for synthesis is simple, effective and reproducible and can be expanded to fabrication of other rare-earth-doped morphology-controlled inorganic nanoparticle materials. High-resolution TEM showed that yttrium-doped CeO_2 with a hollow sphere hierarchical structure is comprised of many small particles with a crystallite size of 30 nm in diameter. The present work showed that yttrium-doped CeO_2 with hollow sphere structure exhibits an advantage of photocatalytic activity. The trend for changes in photocatalytic activity was explained by the oxygen vacancies and surface active oxygen species derived from changing yttrium doping. Compared with octahedral structure CeO_2 with yttrium-doped CeO_2 or without doped, yttrium-doped CeO_2 with a hollow sphere structure exhibits an advantage of photocatalytic activity, due to its higher specific surface area and smaller particle size. The existence of the dopant yttrium provides a higher concentration of oxygen vacancies and can also improve photocatalytic activities of products.

Acknowledgements

The authors are grateful for JST ACT-C program financial and the National Natural Science Foundation of China (No. 51403181).

Appendix A. Supplementary data

Supplementary data associated with this article can be found, in the online version, at <http://dx.doi.org/10.1016/j.cattod.2016.06.049>.

References

- [1] C.-Y. Cao, Z.-M. Cui, C.-Q. Chen, W.-G. Song, W. Cai, *J. Phys. Chem. C* 114 (2010) 9865–9870.
- [2] Y. Chen, T. Liu, C. Chen, W. Guo, R. Sun, S. Lv, M. Saito, S. Tsukimoto, Z. Wang, *Ceram. Int.* 39 (2013) 6607–6610.
- [3] F. Dang, K. Kato, H. Imai, S. Wada, H. Haneda, M. Kuwabara, *Cryst. Growth Des.* 10 (2010) 4537–4541.
- [4] H. Imagawa, A. Suda, K. Yamamura, S. Sun, *J. Phys. Chem. C* 115 (2011) 1740–1745.
- [5] G.-R. Li, D.-L. Qu, L. Arurault, Y.-X. Tong, *J. Phys. Chem. C* 113 (2009) 1235–1241.
- [6] L. Li, H.K. Yang, B.K. Moon, Z. Fu, C. Guo, J.H. Jeong, S.S. Yi, K. Jang, H.S. Lee, *J. Phys. Chem. C* 113 (2008) 610–617.
- [7] M. Lin, Z.Y. Fu, H.R. Tan, J.P.Y. Tan, S.C. Ng, E. Teo, *Cryst. Growth Des.* 12 (2012) 3296–3303.
- [8] T. Mokkelbost, I. Kaus, T. Grande, M.-A. Einarsrud, *Chem. Mater.* 16 (2004) 5489–5494.
- [9] C. Paun, O.V. Safonova, J. Szlachetko, P.M. Abdala, M. Nachtegaal, J. Sa, E. Kleymenov, A. Cervellino, F. Krumeich, J.A. van Bokhoven, *J. Phys. Chem. C* 116 (2012) 7312–7317.
- [10] J.C. Qian, F. Chen, F. Wang, X.B. Zhao, Z.G. Chen, *Mater. Res. Bull.* 47 (2012) 1845–1848.
- [11] W. Shan, H. Guo, C. Liu, X. Wang, *J. Rare Earths* 30 (2012) 665–669.
- [12] G. Shen, Q. Wang, Z. Wang, Y. Chen, *Mater. Lett.* 65 (2011) 1211–1214.
- [13] Z. Wang, Z. Quan, J. Lin, *Inorg. Chem.* 46 (2007) 5237–5242.
- [14] Z.-L. Wang, G.-R. Li, Y.-N. Ou, Z.-P. Feng, D.-L. Qu, Y.-X. Tong, *J. Phys. Chem. C* 115 (2010) 351–356.
- [15] Q. Wu, F. Zhang, P. Xiao, H. Tao, X. Wang, Z. Hu, Y.; Lu, *J. Phys. Chem. C* 112 (2008) 17076–17080.
- [16] J. Xu, J. Harmer, G. Li, T. Chapman, P. Collier, S. Longworth, S.C. Tsang, *Chem. Commun.* 46 (2010) 1887–1889.
- [17] L. Yan, R. Yu, J. Chen, X. Xing, *Cryst. Growth Des.* 8 (2008) 1474–1477.
- [18] S. Yang, L. Gao, *J. Am. Chem. Soc.* 128 (2006) 9330–9331.
- [19] R. Yu, L. Yan, P. Zheng, J. Chen, X. Xing, *J. Phys. Chem. C* 112 (2008) 19896–19900.
- [20] D. Zhang, H. Fu, L. Shi, C. Pan, Q. Li, Y. Chu, W. Yu, *Inorg. Chem.* 46 (2007) 2446–2451.
- [21] R.B. Rakhi, W. Chen, D. Cha, H.N. Alshareef, *Nano Lett.* 12 (2012) 2559–2567.
- [22] F. Wang, H. Dai, J. Deng, G. Bai, K. Ji, Y. Liu, *Environ. Sci. Technol.* 46 (2012) 4034–4041.
- [23] L. Wang, L.-F. Zhang, S.-L. Zhong, A.-W. Xu, *Appl. Surf. Sci.* 263 (2012) 769–776.
- [24] H. Wu, L. Wang, *Catal. Commun.* 12 (2011) 1374–1379.
- [25] Z. Wu, M. Li, S.H. Overbury, *J. Catal.* 285 (2012) 61–73.
- [26] D.-E. Zhang, X.-M. Ni, H.-G. Zheng, X.-J. Zhang, J.-M. Song, *Solid State Sci.* 8 (2006) 1290–1293.
- [27] F. Zhou, X. Ni, Y. Zhang, H. Zheng, *J. Colloid Interface Sci.* 307 (2007) 135–138.
- [28] F. Zhou, X. Wang, X. Sun, Q. Peng, Y. Li, *J. Catal.* 229 (2005) 206–212.
- [29] H. Hojo, T. Mizoguchi, H. Ohta, S.D. Findlay, N. Shibata, T. Yamamoto, Y. Ikuhara, *Nano Lett.* 10 (2010) 4668–4672.
- [30] R. Kostić, S. Aškrabić, Z. Dohčević-Mitrović, Z.V. Popović, *Appl. Phys. A* 90 (2007) 679–683.
- [31] Y. Lee, G. He, A.J. Akey, R. Si, M. Flytzani-Stephanopoulos, I.P. Herman, *J. Am. Chem. Soc.* 133 (2011) 12952–12955.
- [32] D.R. Mullins, P.M. Albrecht, T.-L. Chen, F.C. Calaza, M.D. Biegalski, H.M. Christen, S.H. Overbury, *J. Phys. Chem. C* 116 (2012) 19419–19428.
- [33] Z. Wu, M. Li, J. Howe, H.M. Meyer 3rd., S.H. Overbury, *Langmuir* 26 (2010) 16595–16606.
- [34] S.C. Yan, Z.S. Li, Z.G. Zou, *Langmuir* 26 (2010) 3894–3901.
- [35] F. Zhang, *J. Appl. Phys.* 95 (2004) 4319.
- [36] Y. Ma, X. Wang, S. Li, M.S. Toprak, B. Zhu, M. Muhammed, *Adv. Mater.* 22 (2010) 1640–1644.
- [37] R. Srinivasan, A. Chandra Bose, *Mater. Lett.* 64 (2010) 1954–1956.
- [38] N. Wetchakun, S. Chaiwichain, B. Inceesungvorn, K. Pingmuang, S. Phanichphant, A.I. Minett, J. Chen, *ACS Appl. Mater. Interfaces* (2012).
- [39] S. Yang, Y. Guo, H. Chang, L. Ma, Y. Peng, Z. Qu, N. Yan, C. Wang, J. Li, *Appl. Catal. B: Environ.* 136–137 (2013) 19–28.
- [40] Z.-X. Li, L.-L. Li, Q. Yuan, W. Feng, J. Xu, L.-D. Sun, W.-G. Song, C.-H. Yan, *J. Phys. Chem. C* 112 (2008) 18405–18411.
- [41] M. Machida, Y. Murata, K. Kishikawa, D. Zhang, K. Ikeue, *Chem. Mater.* 20 (2008) 4489–4494.
- [42] E.W. McFarland, H. Metiu, *Chem. Rev.* (2013).
- [43] B. Xu, Q. Zhang, S. Yuan, M. Zhang, T. Ohno, *Appl. Catal. B: Environ.* 164 (2015) 120–127.
- [44] B. Xu, Q. Zhang, S. Yuan, M. Zhang, T. Ohno, *Appl. Catal. B: Environ.* 183 (2016) 361–370.
- [45] B. Xu, Q. Zhang, S. Yuan, M. Zhang, T. Ohno, *Chem. Eng. J.* 260 (2015) 126–132.
- [46] Q.zhang S.s.yuan, B. Xu, *RSC Adv.* (2014) 127.
- [47] K. Vasanth Kumar, K. Porkodi, F. Rocha, *Catal. Commun.* 9 (2008) 82–84.
- [48] Lun Pan, Ji-Jun Zou, Xiangwen Zhang, Li Wang, *J. Am. Chem. Soc.* 133 (2011) 10000–10002.